Error Budget of Inverse Box Models: The North Atlantic

ALEXANDRE GANACHAUD

Institut de Recherche pour le Développement, Laboratoire d'Etudes Geophysiques et d'Oceanographie Spatiale–UMR5566/CNRS/CNES/IRD/UPS, Nouméa, New Caledonia

(Manuscript received 29 March 2002, in final form 21 March 2003)

ABSTRACT

Linear inverse box models based on hydrographic data are widely used to estimate the ocean circulation and associated transports of heat and of other important quantities. The inverse method permits calculation of a circulation that is consistent with basic conservation laws such as those for mass or salt along with uncertainties. Both uncertainties and solution depend upon assumptions about noise and the limitations of linear models. Internal waves introduce noise into the measurements, while ocean variability sets bounds on the linear model skills when time average circulation is sought. Observations of internal wave spectra and sensitivity experiments on hydrographic data suggest estimates for measurement errors in transport calculations of ± 3 Sv (1 Sv $\doteq 10^6$ m^3 s^{-1} $\simeq 10^9$ kg s^{-1}) at midlatitudes, with dependence on latitude. The output of a realistic numerical ocean model is used to quantify the impact of ocean variability on one-time hydrographic sections. The implied error is of order ± 8 Sv in net mass balance and ± 100 kmol s^{-1} in net silica balance. (The estimates are a priori errors.) Net mass balance has often been assumed more accurate with errors in individual layers compensating. While this may be true instantaneously, it is shown here that such an assumption leads to incorrect estimation of the time mean transports and diapycnal transfers.

1. Introduction

So-called ''inverse box models,'' first described by Wunsch (1978), are now commonly used to estimate the ocean circulation and transports using hydrographic data (e.g., Macdonald and Wunsch 1996; Robbins and Toole 1997; Tsimplis et al. 1998; Ganachaud and Wunsch 2000). These models provide a formal link among data, ocean dynamics, and a priori knowledge of the circulation. Sets of temperature, salinity, and sometimes oxygen and nutrient measurements at depth and across a transoceanic section are used to obtain a best estimate of the velocity field and property transports, along with an estimate of their respective uncertainties. From temperature and salinity measurements, the geostrophic flow (thermal wind) is calculated relative to a given reference surface. This ''dynamic method'' usually employs the reference surface as one where the initial velocity estimate is zero. In practice, any additional information, such as that from current meters, can be employed to establish the initial velocity at the reference surface (''reference velocity''). The thermal wind integrated from that reference gives an initial estimate of the general circulation, but one which usually fails to satisfy basic requirements (''constraints'') such as mass, heat, and salt conservation. Modifications are made to the reference velocities (and any other adjustable parameters) so as to force the circulation to consistency with the unsatisfied requirements.

However, because of the existence of noise and incomplete physics in the geostrophic model, no constraint should be satisfied exactly. The solution depends directly upon the degree to which the constraints are satisfied, and one must attempt to be as realistic as possible in estimating the expected error in any requirement. The purpose of this paper is to reexamine from the beginning the question of noise in hydrography, and to provide zero-order, but nonetheless fully quantitative, values. Mass conservation is the most basic, and usually the most important, of all imposed constraints; it is also representative of other conservation requirements. We also briefly examine tracer conservation constraints, using silicate as the example.

Few estimates of prior uncertainties are available. Roemmich (1980) estimated that total mass could be conserved within ± 1 to ± 2 Sv (1 Sv $= 10^6$ m^3 s^{-1}) between two trans-Atlantic sections without incurring large changes to the initial circulation. Several studies ''tested'' the ability of inverse models to reproduce a numerical ocean circulation with various inverse models (Zhang and Hogg 1996), with success depending upon both model and constraints. For instance, McIntosh and Rintoul (1997) applied the method to an instantaneous snapshot of the Southern Ocean circulation from a qua-

Corresponding author address: Dr. Alexandre Ganachaud, Institut de Recherche pour le Développement, Centre de Nouméa, Nouméa BP A5, New Caledonia.
E-mail: ganacho@noumea.ird.nc

si-eddy-resolving general circulation model (GCM). They found that the inverse calculation was successful as long as the prior statistics of the solution corresponded to the correct (i.e., GCM) solution, as linear estimation theory shows must be true. They did not include any measurement noise and constrained mass to be conserved within ± 0.01 Sv which would be unrealistic for real data.

The full inverse problem for a box model is a nonlinear one (Mercier 1986; Wunsch 1994) because one could permit modification of the underlying temperature and salinity fields to correct for time changes or measurement errors. By fixing the temperature and salinity, the problem is linearized, but one introduces a residual error into the calculation. This error is estimated here in the North Atlantic.

Section 2 presents the formalism of the problem and basic notations; section 3 gives estimates of the effect of oceanic variability on one-time sections; section 4 quantifies the various measurement noise sources; section 5 provides values for the a priori size of the solution (reference velocities); while section 6 analyzes the conservation of silicate, followed by a general discussion and summary of the error budget.

2. Formalism

Consider a zonal hydrographic section. The geostrophic velocity field between pairs of stations is derived from thermal wind,

$$\begin{aligned} v_a(x, z) &= v_R(x, z) + b(x) \\ &= -\frac{g}{\rho_0 f}\int_{z_0(x)}^{z}\frac{\partial \rho}{\partial x}\,dz + b(x), \end{aligned} \tag{1}$$

where z is the vertical coordinate (increasing upward); x is the horizontal coordinate along the section; $z_0(x)$ is an arbitrary reference depth; $v_a(x, z)$ is the absolute velocity, $v_R(x, z)$ is the thermal wind relative to $z_0(x)$ and $b(x)$ is the unknown reference velocity at $z_0(x)$ (or a correction to an optimal guess); g is gravity; and f is the Coriolis parameter. The ''reference surface'' $z_0(x)$ is specified at each pair according to prior knowledge. Both b and v are normal to the section and represent horizontal averages between the stations. The initial circulation is inferred by elaborate guesses of the reference surface, $z_0(x)$, at which $b(x)$ would almost vanish. The inverse calculation provides an estimate of the adjustment $\{b_i\} = \mathbf{b}$ to this a priori solution, along with its error covariance $\mathbf{P}$. This solution satisfies the constraints on the circulation and is consistent with the a priori variance of $\mathbf{b}$. (Bold lowercase letters represent column vectors, while bold uppercase letters are matrices.)

The net transport of a tracer C is a linear combination of b and v_R,

$$\begin{aligned} T &= \int_{\text{West}}^{\text{East}} dx \int_{\text{Bot}(x)}^{\text{Top}(x)} dz\ \rho(x, z)C(x, z) \\ &\quad \times [b(x) + v_R(x, z)] \\ &= T_b + T_R, \end{aligned} \tag{2}$$

where C is the tracer concentration per unit mass ($C = 1$ for mass), T_b is the reference velocity contribution, and T_R is the contribution from relative velocities. For individual oceanic layers, Top(x) and Bot(x) define the upper and lower boundaries of the layer. Steady-state mass conservation may be written

$$\nabla\cdot(\rho\mathbf{v}) = \text{FW},$$

where $\mathbf{v}$ is the three-dimensional velocity vector and FW is the net freshwater flux into the area (hereafter, FW = 0 for simplicity). The corresponding equation for tracers is

$$\nabla\cdot(\rho C) = \nabla\cdot\kappa\nabla(\rho C) + Q, \tag{3}$$

where κ is an eddy diffusion tensor and Q is a possible source or sink. It is assumed that the spatial sampling along a section is fine enough to resolve most of the horizontal eddy tracer transport; that is, smaller-scale lateral processes including horizontal diffusion are contained in the noise. Integrated over a layer bounded horizontally by zonal hydrographic sections and land, and vertically by isopycnal surfaces, and rearranged, (3) becomes (appendix A)

$$\mathbf{a}^{\mathrm{T}}\mathbf{x} + n = y \tag{4}$$

with

$$\mathbf{x} = \begin{bmatrix} \{b_i\}_{i=1,N_p} \\ \{w_k^*\}_{k=1,N_l-1} \\ \{\kappa_k^*\}_{k=1,N_l-1} \end{bmatrix},$$

where $\mathbf{x}$ contains the unknowns b_i at each station pair and diapycnal transfers $\{w_k^*\}$ and $\{\kappa_k^*\}$, and $\mathbf{x}$ can include other parameters such as adjustments to Ekman transport at the surface or freshwater transport; N_p is the number of station pairs; N_l the number of layers and; $\mathbf{a}$ is the discrete integrals of T_b and of dianeutral transfers. The term y contains the relative transport divergence (T_R) and the source term Q, including the Ekman transport convergence. As (4) cannot be satisfied exactly with real data, n represents the noise. Equations of the form (4) for different layers and properties are grouped to form a single matrix equation,

$$\mathbf{E}\mathbf{x} + \mathbf{n} = \mathbf{y}, \tag{5}$$

where $\mathbf{E}$ is M equations $\times N$ unknowns. Constraints on net transports in particular regions (e.g., Florida Strait) are added by choosing appropriate elements for $\mathbf{E}$ and $\mathbf{y}$. Various methods have been used to solve (5) for $\mathbf{x}$ and $\mathbf{n}$, with corresponding solutions and uncertainties depending on the a priori knowledge that one has on their size. While the dependence is formally specified

via the covariance matrices for methods such as Gauss–Markov (Wunsch 1996), the a priori knowledge will guide the author to choose a solution, that is, the rank for the singular value decomposition method.

At any time t, and assuming geostrophy, net mass transport $T(t)$ through a section is the sum

$$T(t) = T_b(t) + T_R(t) + T_{\mathrm{Ek}}(t), \tag{6}$$

with

$$T_{\mathrm{Ek}}(t) = -\int_{X_W}^{X_E} dx\, \rho\, \frac{\tau^x(t)}{f}, \tag{7}$$

where $T_{\mathrm{Ek}}(t)$ is the near-surface Ekman transport and $\tau(t)^x$ is the zonal wind stress. It takes 1–3 months to make a transoceanic section; and sections used in a box model may be separated in time by several years. What is sought here is the time-mean transports across all data involved,

$$\overline{T} = \overline{T}_b + \overline{T}_R + \overline{T}_{\mathrm{Ek}}, \tag{8}$$

where the overbar denotes a time average. Because $\overline{T}_R$ is based on a quasi-synoptic measurement (say, at time t_0), the existence of a mass conserving solution relies on the assumption that $T_R(t_0) \simeq \overline{T}_R$ to a good approximation. In contrast, $\overline{T}_{\mathrm{Ek}}$ can be calculated from meteorological wind fields, while $\overline{T}_b$ is estimated by the inverse model. Write n^v as the corresponding error due to variability, then

$$\begin{aligned} \overline{T}_R &= T_R^c(t_0) + n^v, \\ &= T_R^m(t_0) + n^m + n^v, \end{aligned} \tag{9}$$

Here, the c superscript is the correct value and the m superscript implies a measurement. The error n^m due to measurements, discussed later, comes from internal wave noise, ''bottom triangles,'' etc., and n^v reflects the inability of the linearized model to modify the vertical shear. In a more elaborate inverse model like the ones of Mercier (1986), change is allowed in the density field, thus reducing the model error. Because no such change is allowed here, any noise in T_R may lead to a net mass imbalance in the solution.

3. Variability and model error

The error n^v is estimated with the help of a near-eddy-resolving GCM from the U.S. Naval Post Graduate School (see Semtner and Chervin 1992; Stammer et al. 1996, hereafter STSW96). The 1/4° horizontal resolution configuration the Parallel Ocean Circulation Model, version 4B [(POCM-4B)] has 20 vertical levels and was forced with daily wind stress fields from the European Centre for Medium-Range Weather Forecasts (ECMWF). Surface temperature and salinity were restored to the Levitus et al. (1994) and Levitus and Boyer (1994) monthly fields with a 30-day timescale. The GCM was integrated for 8 yr (1987–94) and forced seasonally with repetitive climatological temperature, salinity, and heat transports so that interannual forcing comes from the wind fields. As a result, variability in the meridional overturning circulation is a lower bound on the true amplitudes (STSW96). Nevertheless, model drift introduces additional spurious variability. STSW96 found that the GCM reproduced successfully the major features of the large-scale oceanic circulation and the variability structure compared with altimetric and hydrographic observations. The variability amplitude is underestimated by at least a factor of 2–4 on most scales with highest discrepancy in the mesoscale range. It is not clear how well the respective fractions of baroclinic and barotropic variability are represented. The GCM variability was not evaluated at depth by STSW96.

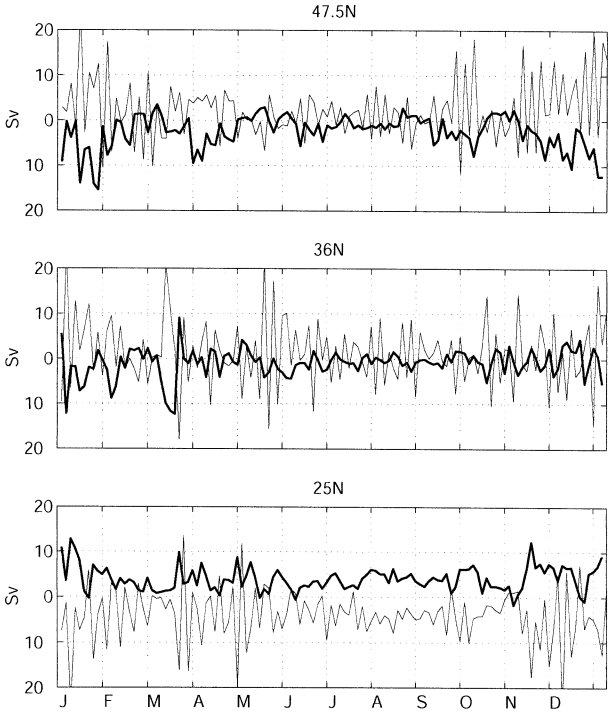

FIG. 1. Time series of the meridional Ekman flow (thick line) and the integrated model flow beneath 100 m (thin line) across the Atlantic at 47.5°, 36°, and 24°N. High-frequency inertial oscillations are part of the model response. The two curves nearly cancel each other when high frequencies are filtered out (not shown).

a. Ekman transport fluctuations

Temperature, salinity, velocity, and sea surface height data were subsampled every third day for the 8-yr period at three latitudes corresponding to actual hydrographic data in the Atlantic Ocean: 25°, 36°, and 48°N. Meridional Ekman transport was computed from the wind stress and the conventional Ekman formula (7) (Fig. 1, thick line). Variations are fast with variations of up to 30 Sv in a few days. In Fig. 1 the total flow beneath 100 m is overlaid. If high frequencies (inertial oscillations) are filtered out, the imbalances do not exceed ±0.8 Sv rms (not shown), showing that (7) is an ac-

TABLE 1. Potential density interfaces.

σ_θ*	σ_2*	σ_4*
26.4	36.87	45.81
26.8	36.94	45.85
27.1	36.98	45.87
27.3	37.02	45.895
27.5		45.91
27.7		45.925

* Sigma is referenced to the surface, 2000 db, and 4000 db.

curate approximation to the GCM boundary layer and that there is no storage of important quantities of water by elevation of the sea surface. A calculation of net transport, including the surface layer and across 36° and 48°N, revealed no change in mass storage between those latitudes exceeding ±0.2 Sv.

Fast variations in Ekman mass transports are therefore instantaneously compensated by an interior flow in the opposite direction, and, because this return flow is depth independent, there is no perturbation in the density field. Ganachaud and Mercier (2002) obtained similar results from a different numerical model and showed that the response was not only barotropic, but also geostrophic in the Atlantic Ocean. Therefore, different hydrographic sections can be consistently combined in an inverse box model as long as the time-mean Ekman transport is used for all sections. This balance was observed in the repeat observations of Roemmich et al. (2001), which showed no significant correlation between annual fluctuations of Ekman and relative transports in the upper, midlatitude Pacific Ocean, and only weak correlations at interannual timescales where the response is expected to be more baroclinic (Willebrand et al. 1980). Near the equator, the response is also more baroclinic, and the low-latitude behavior is postponed as a possible extension of this work.

The accuracy of the time-mean Ekman transport is difficult to assess. Local measurement buoys have shown that (7) was a good approximation for quiet wind conditions (Schludlich and Price 1998). On large scales and with varying winds, existing measurements from ship acoustic Doppler current profiler (ADCP) are more uncertain although in agreement with (7) (e.g., Chereskin and Roemmich 1991). The wind stress accuracy is also difficult to assess. Comparison between different wind fields shows deviations of up to 46% (Mestas-Nuñez et al. 1994; Roemmich et al. 2001) for high winds. An uncertainty of 20%–50% for the time-mean Ekman transport is probably a realistic, zero-order ''guess.''

b. Baroclinic variability n^v

Locally, mesoscale baroclinic eddies introduce large deviations from the mean transport, so that estimating the time-average thermal wind flow would require an enormous dataset. Integrated on large spatial scales,

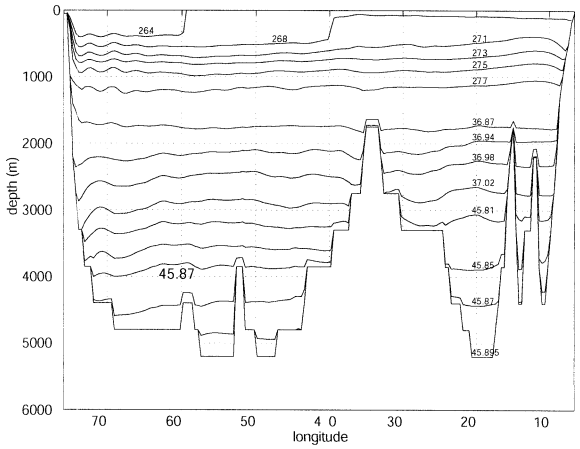

FIG. 2. Isopycnal interface position at 36°N. For simplicity, interface depths were computed without allowing changes in the reference pressure, in contrast to Macdonald's definition. [In the Macdonald (1998) definition a reference pressure is assigned to an isopycnal at one end of a hydrographic section. The isopycnal position is computed along the section. If the isopycnal deviates too much from the original reference, the local reference pressure is changed to continue the calculation along the section.]

those fluctuations tend to cancel out. The corresponding variability in T_R is estimated from the GCM, first by assuming numerical ''hydrographic sections'' are instantaneous, then simulating the finite duration of a real cruise [section 3b(1)]. The thermal wind v_R is calculated [(1)] from the GCM temperatures and salinities. The velocity is referenced to the same isopycnal surfaces as Macdonald (1998): $\sigma_4 = 45.81$ at 25° and 36°N (a depth of approximately 3000 m), and $\sigma_2 = 36.87$ at 48°N (1500–2000 m). The relative geostrophic transport is integrated in the layers of Table 1 as in Macdonald (1998) and predecessors (Fig. 2 gives a snapshot at 36°N). Neutral surfaces (McDougall 1987) would be more consistent with the Macdonald definition, but their computation is too time consuming for repetition. The calculation was repeated every third day for 8 yr [the relative geostrophic velocity spectrum is sufficiently red that aliasing of high frequencies is not of concern (Jayne and Tokmakian 1997)]. In the GCM, the balance (6) could not be evaluated because it was not possible to calculate accurately enough the depth-independent part of the absolute geostrophic velocity with the fields that were available to us (appendix A of Ganachaud 1999). A similar analysis on the recent CLIPPER model (1/6°, Atlantic Ocean) confirms the validity of (6) to within less than 2 Sv in the North Atlantic (Ganachaud and Mercier 2002).

Figure 3 shows, the time-mean transport from the relative velocity (T_R) across latitudes 25°, 36° and 48°N along with its variability (shaded, one standard deviation). The layer thicknesses reported correspond to a zonal average. The relative transport variability is largest in the surface layers, with ±1 to ±2 Sv rms, while it generally does not exceed ±0.5 Sv rms below 2000

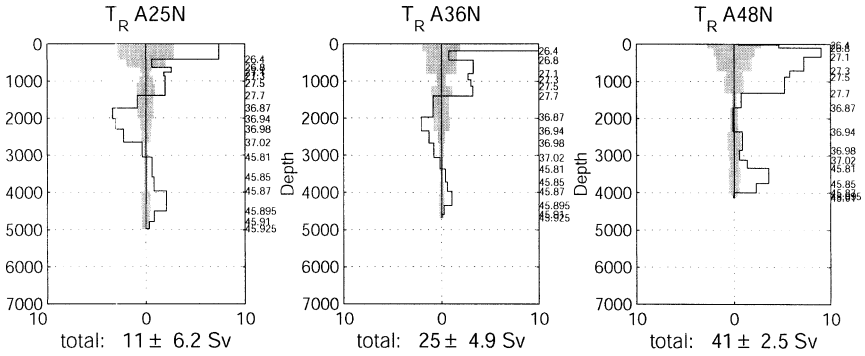

FIG. 3. Relative mass transport in individual layers at (left) 25°, (middle) 36°, and (right) 48°N in the GCM. The 8-yr average is indicated by the lines while the variability is given by the shaded area (one std dev).

m. Variability in the deep layers increases at 48°N in the 2000–4000-m range, either due the shallower reference surface chosen there, or to a natural deep variability (Koltermann et al. 1999). The variability in the net relative transport (values below graphics) ranges ±2.5 Sv rms (48°N), ±5 Sv rms (36°N), and ±6 Sv rms (25°N).

A theoretical study of seasonal variability by Gill and Niller (1973) predicted a relatively small and barotropic response away from the equator. At 24° and 36°N, repeat hydrographic sections were obtained in the late 1950s, 1981, and the early 1990s. Shifts in the water mass characteristics have been found (e.g., Bryden et al. 1996; Arbic and Owens 2001). However, Roemmich and Wunsch (1985) obtained little difference between the absolute geostrophic transports from the 1950s and 1981 with deviations on the order of 1 Sv in individual layers (as in Table 1), with larger deviations near the surface. Those differences could accumulate vertically to 7 Sv over consecutive layers. At 24°N, Lavin (1993) did a similar comparison including a 1992 occupation. Top-to-bottom geostrophic transports on the three occupations from Bahamas to Africa referenced to 1100 m showed deviations of +9.3 Sv (1957 → 1981) and −5.2 Sv (1981 → 1992). These magnitudes are consistent with our ±6 Sv GCM variability in the total transport at 24°N (referenced to a deeper surface). At 24°, 36°, and 48°N, Koltermann et al. (1999) did similar comparisons, but because they used the extreme assumption of oceanic Sverdrup balance to the seafloor (Luyten et al. 1985), their results cannot be used to distinguish the variability that is due to changes in the density field apart from the barotropic (and Sverdrup contaminated) part. In the Pacific Ocean at 24°N, the variability of the upper-800-m T_R was evaluated at ±2–3 Sv rms from 28 repeat, high-resolution expendable bathythermograph/expendable conductivity–time–depth (XBT/XCTD) measurements (Roemmich et al. 2001), again consistent with our Atlantic results.

c. One-month sections

Because it takes approximately 1 month for a ship to cross the Atlantic, the field observed by the ship is different from any instantaneous field. For instance, eddies moving with the ship exhibit smoother gradients than those moving against it. To explore this ''cruise aliasing'' effect, 1-month-long cruises were simulated along 36°N in the GCM, from west to east and for each month of 1993. Layer transports did not show departures from the 1993 average that would exceed the natural variability reported in the preceding section. Still, the effect of aliasing increases the top-to-bottom thermal wind transport variability: at 36°N, T_R varied by ±4.8 Sv rms between the 12 cruises versus ±3.5 Sv rms from 3-day snapshots. This additional bias does not exceed the ±5 Sv rms 8-yr variability there, and for this ''order of magnitude'' error budget, cruise aliasing does not introduce a large error compared to that of natural variability. As 36°N is a typical mid-Atlantic regime, we anticipate the situation to be similar at the two other latitudes.

A second kind of aliasing is caused by finite station separation. Much of the eddy energy occurs on scales comparable to station spacing (generally close to the first Rossby radius), and variability on scales less than that distance is aliased. The GCM output is inadequate to quantify this error because subsampling the GCM fields incurs errors from the representation of the bottom topography. Roemmich and Wunsch (1985) compared the transports from two coarse-resolution and two fine-resolution sections taken at different times in the North Atlantic and concluded that temporal variability dominated the differences in geostrophic transports. This aliasing, however, could be better quantified using higher-resolution models and high-frequency observations such as XBTs, current meters, and altimetry. Recent experiments on high-resolution numerical models suggest that a hydrographic resolution of 50 km may lead to an underestimation of property transports by eddies

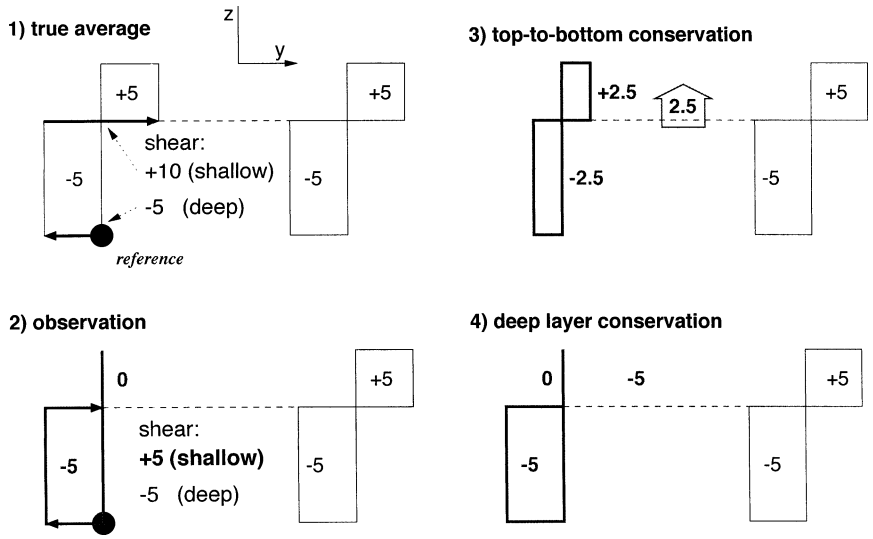

FIG. 4. Enhancing conservation in the deep layers at the expense of the top-to-bottom mass budget: a simplified example with two hydrographic sections. Panel 1 shows the true average circulation thermal wind with an appropriate reference level taken at the bottom for both sections. Panel 2 shows a one-time observation of the thermal wind, which gives a different shallow shear in the left section, i.e., a 5-Sv error with respect to the time average. The right section is supposed steady and accurately measured. Panels 3 and 4 are adjustments to the initial circulation (panel 2), one that conserves mass top to bottom (panel 3) and the other one that conserves mass in the deep (panel layer 4). In case 3, spurious diapycnal transfers are diagnosed.

(P. Klein 2001, personal communication; and Levy et al. 2001).

d. Application to inverse models

Hydrographic measurements simulated in a numerical model show that variations in Ekman transport have little impact on the density field and that the variability in the density field introduces an uncertainty in the relative thermal wind transport of ± 0.1 to ± 2 Sv in (our) isopycnal layers that adds up to ± 5 Sv top to bottom.

Because at any time the top-to-bottom baroclinic transport $T_R(t)$ is balanced by depth-independent changes, it is tempting to impose strict top-to-bottom conservation when combining zonal sections taken at different times (assuming the objective is to estimate the time-mean flow). Figure 4 illustrates the consequences of such constraints in a simplified case. The true average is an overturning of 5 Sv [Fig. (4.1)]. Because of baroclinic variability in the upper layer, a shear of 5 Sv instead of 10 Sv is observed in the left section [Fig. (4.2)]. (The right section is supposed steady for this illustration purpose although its circulation would also change in practice.) If one enforces top-to-bottom mass conservation across the two sections, the circulation [Fig. (4.3)] is estimated at half the overturning strength and spurious vertical transfers appear across isopycnals to accommodate the difference between the horizontal transport at the two sections. The weak overturning on the left truly represents the instantaneous circulation at the time of the section; it is nonetheless a misrepresentation of the time mean, leading to those vertical transfers. But the GCM simulation and repeat observations show that $T_R(t)$ is more stable in the deep layers, suggesting that one should require a closer mass conservation in the deep layers at the expense of top-to-bottom conservation. This yields a circulation that is representative of the time average but contains residual mass divergences in the upper layer, and top to bottom [Fig. (4.4)]. This solution is correct as long as the total mass residuals are indistinguishable from zero within uncertainties.

4. Measurement noise

The measurement noise n^m derives from both the temperature/salinity measurements and from approximations done in transport calculations. Errors in navigation, instruments, and internal waves all contribute to contaminate the data. Navigation is today only a minor error source. Moreover, errors in station positions tend to cancel out in geostrophic transport computations. CTDs have reached an absolute accuracy of approximately 10^{-3} K for temperature and better than 4×10^{-3} for salinity when carefully calibrated (Saunders 1986). [World Ocean Circulation Experiment (WOCE) standards require 0.005-K accuracy and 0.002-K precision (Joyce and Corry 1994).] The corresponding noise in the density is 3×10^{-4} kg m^{-3} from temperature noise (10^{-3} K) and 3×10^{-3} kg m^{-3} from salinity noise (4×10^{-3}). Improper calibration may introduce biases of ± 0.01 K in temperature and ± 0.01 in salinity (Marotzke

and Willebrand 1996, p. 64), causing uniform density shifts with no effect on geostrophic transports.

a. Internal waves

The transport due to the geostrophic velocity referenced to the bottom between any station pair S_w and S_e may be written

$$T = \int_{S_w}^{S_e} dx \int_{-h}^{0} dz\, v(x, z)$$
$$= -\int_{S_w}^{S_e} dx \int_{-h}^{0} dz \int_{-h}^{z} d\zeta \frac{g}{\rho_0 f} \frac{\partial \rho(x, \zeta)}{\partial x}, \quad (10)$$

where ζ is a dummy depth variable and h is bottom depth. For constant depth, T depends only upon the density measurements at S_w and S_e:

$$T = \frac{g}{\rho_0 f} \int_{-h}^{0} dz \int_{-h}^{z} d\zeta [\rho(S_w, \zeta) - \rho(S_e, \zeta)]. \quad (11)$$

Because internal waves move isopycnals in a nongeostrophic manner, the measured isopycnal position is in error (n_ρ) with respect to its geostrophic position. This implies an error n^m in T:

$$n^m = -\frac{g}{\rho_0 f} \int_{-h}^{0} dz \int_{-h}^{z} d\zeta [n_\rho(S_w, \zeta) - n_\rho(S_e, \zeta)], \quad (12)$$

with variance

$$\langle (n^m)^2 \rangle = \left(\frac{g}{\rho_0 f}\right)^2 \int\int_{-h}^{0} dz\, dz' \int_{-h}^{z} \int_{-h}^{z'} d\zeta\, d\zeta'$$
$$\times \langle [n_\rho(S_e, \zeta) - n_\rho(S_w, \zeta)]$$
$$\times [n_\rho(S_e, \zeta') - n_\rho(S_w, \zeta')] \rangle,$$

where the bracket $\langle \cdot \rangle$ denotes the expected value.

Observations show no evidence of horizontal coherence over distances larger than 10 km (Garrett and Munk 1972), and one can assume that $n_\rho(S_w)$ and $n_\rho(S_e)$ are uncorrelated. We then have

$$\langle (n^m)^2 \rangle = \left(\frac{g}{\rho_0 f}\right)^2 \int_{-h}^{0} dz \int_{-h}^{0} dz' \int_{-h}^{z} d\zeta \int_{-h}^{z'} d\zeta$$
$$\times [2 \times \langle n_\rho(\zeta) n_\rho(\zeta') \rangle]. \quad (13)$$

The water column is divided into segments Δz_i of 500 m or more so that the internal wave noise is approximately uncorrelated between each segment. The covariance matrix $\langle n_\rho(z_i) n_\rho(z_j) \rangle$ is diagonal with elements chosen for each depth following Marotzke and Willebrand (1996) with slight modifications. The variance of the isopycnal displacements is estimated from Munk (1981):

$$\langle \xi^2 \rangle = 53 \frac{N_0}{N(z)} \quad (\mathrm{m}^2),$$

so that

$$\langle n_\rho^2 \rangle = 53 \left(\frac{\rho_0}{g}\right)^2 \times N_0 N(z)^3, \quad (14)$$

where $N_0 = 5.2 \times 10^{-3}\ \mathrm{s}^{-1}$ and N is the local buoyancy frequency. Here, N varies from $0.8 \times 10^{-3}\ \mathrm{s}^{-1}$ in the deep layers to $5 \times 10^{-3}\ \mathrm{s}^{-1}$ in the thermocline at midlatitudes (Gill 1982, p. 52). The corresponding noise n_ρ ranges from 0.0013 to 0.02 kg m^{-3} rms. In the deep ocean, n_ρ is given a lower bound equivalent to the CTD noise (0.003 kg m^{-3} rms). At a latitude of 30° and for $h = 4000$ m, the resulting rms noise in the transport is

$$\langle (n^m)^2 \rangle = (\pm 3 \text{ Sv rms})^2. \quad (15)$$

A depth of $h = 5000$ m produces a similar result. The Coriolis parameter controls the size of $\langle (n^m)^2 \rangle$. Fieux et al. (1996) observed transport fluctuations on the order of 9 Sv between stations repeated a few hours apart near Bali and suspected internal wave activity. At their latitude, (12) predicts a noise of the same order, ±10 Sv.

b. Geostrophy

Away from the Ekman layer, geostrophy is a good approximation. Even in western boundary currents, scaling shows near-geostrophic balance (e.g., Pedlosky 1987, ch. 8) apart from simple cyclostrophic corrections. Observational tests have failed to detect significant deviations from geostrophy anywhere outside the surface layers (Wunsch 1996, ch. 2). Johns et al. (1989) showed that in a strong curve of the Gulf Stream the cyclostrophic term introduces an ageostrophy of up to 2 Sv. Ageostrophic motions also include the widely observed energetic inertial oscillations. These motions do not affect hydrographic measurements and their transports of scalar oceanic properties are negligible: for a surface inertial velocity of order $V = 10\ \mathrm{cm\ s}^{-1}$, inertial circles have a radius $R = V/f = 1000$ m at midlatitudes and a westward Stokes drift of (Ripa 1997)

$$\langle \dot{x} \rangle = -\frac{1}{2} \beta R^2 \sim 0.5 \times 10^{-1} \times 10^6$$
$$= O(5 \times 10^{-4}\ \mathrm{cm\ s}^{-1}),$$

where β is the planetary vorticity gradient. The value, $5 \times 10^{-4}\ \mathrm{cm\ s}^{-1}$, is much smaller than ambient geostrophic flows.

c. Bottom triangle

To compute geostrophic transports between two stations over a sloping bottom, properties must be extrapolated below their deepest common level (DCL). As shown in Fig. 5 the extrapolation might be done along the bottom slope or equivalently on the imaginary points (in white) below the DCL at the shallow station. The corresponding temperatures are denoted T_{shal} and the ones of the deep station T_{deep} (black points), with salin-

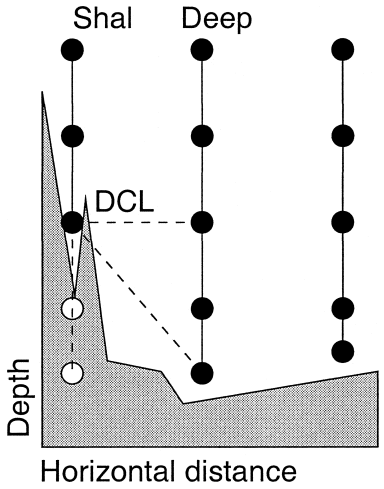

FIG. 5. Bottom triangle problem. The topography is shaded; the left vertical line is a shallow station; the right line is a deep station. Black dots are temperature.

ities S_{shal} and S_{deep}. Uncertainties arise from extrapolation and from estimation of the area in the bottom triangle.

Six common extrapolation methods are compared here. 1) Null velocity assumes the transport in the triangle vanishes. 2) No shear has $T_{shal}(z) = T_{deep}(z)$ with constant geostrophic velocity below the DCL. 3) In constant slope, T_{shal} is computed so that the isotherm slopes are the same as above the DCL. The slope magnitudes are arbitrarily limited to exclude excessively large shears. For our experiments a maximum slope of 1 was allowed [slope $= (T_k^{i+1} - T_k^i)/(T_{k+1}^i - T_k^i)$] to reproduce procedures used in the past (e.g., Macdonald 1998) (here k is the vertical increment, i the station number). 4) In the planar fit method (Wunsch 1996), a linear function $T(x, z) = ax + bz + c$ is determined by regression on the data. The relation gives T_{shal}. 5) In the polynomial fit method, $T(x, z) = ax + bz + cz^2 + d$, useful in regions of strong T stratification. 6) The horizontal method involves extrapolation from the next deeper station. The relative geostrophic transports were computed from *real* hydrographic data using methods 1–6 across 24°, 36°, and 48°N. We used the same reference isopycnal as in section 3b or the bottom if shallower than the target isopycnal. For those ''shallow stations,'' the velocity is referenced either at the depth of the deepest station or at the DCL of the two stations. The resulting transports are displayed in Fig. 6.

If the reference level is taken at the deepest stations (Fig. 6, upper panel) the relative transports vary from 6 to 31 Sv at 24°N depending upon the method with largest deviations of 45 Sv at 36°N between methods 3 and 6. The discrepancies appear almost exclusively in regions shallower than the reference isopycnal. Because velocity is referenced to the deepest station, errors in the bottom triangle are then propagated through the whole water column. An extreme occurs along the eastern side of 36°N where the strong density gradient between 1000 and 2000 db coincides with a steep bottom so that the shear in the bottom triangle varies by 1 m s^{-1} from one method to the next. The associated transport deviations reach 30 Sv with ''constant slope.'' While such an extreme is readily identified, smaller errors are impossible to detect.

To minimize the bottom triangle error, we reference the thermal wind to the DCL instead of the deepest station so that the extrapolation does not affect velocity above the DCL. (In the case of a reference isopycnal between the DCL and the deepest station, the reference was taken at the DCL.) Figure 6 (lower panel) shows that within 1 Sv, except for the polynomial fit at 24°N, the relative transports are independent south of 48°N. At 48°N, the scatter is more important (4–9 Sv) because the deep western boundary crosses several bottom triangles.

Because methods 2–5 propagate the temperature structure downward, they can introduce unrealistic temperature gradients for large bottom slope. Method 1 (null transport) is unrealistic as well, as it implies a discontinuous shear at the DCL. The ''constant velocity'' method implies an abrupt flattening of isopycnals. Horizontal extrapolation appears to be the most physical, as it reproduces the velocity shear from the next station pair and at same depth although it may be unstable in the rare case of two closely spaced stations followed by a distant station along a rising bottom slope.

The error due to the bottom triangle is therefore of order 1 Sv as long as the reference level of shallow stations is taken at DCL (Fig. 6, lower panel). Experiments on many hydrographic sections (Ganachaud and Wunsch 2000) show that horizontal extrapolation yields the most stable results. In a boundary current along sloping topography, this error increases to 2–4 Sv, and probably more in overflow regions. Because we compared various extrapolation methods with a null bottom triangle transport, we may overestimate the actual error. Further tests may narrow the uncertainty in specific situations, for example, subsampling a high-resolution section or numerical model or comparing calculations with adequate lowered ADCP (LADCP) measurements.

5. Reference velocity magnitude

To analyze the expected size and variability of the reference velocities, they were calculated from the time-mean absolute geostrophic velocity (thermal wind plus surface pressure gradient) in the GCM (at the reference isopycnals of section 3b). In principle, the full reference velocity covariance, $\langle \mathbf{b}\mathbf{b}^{\mathrm{T}} \rangle = \langle b(x)b(x') \rangle$, could be derived from the GCM. However, because $\langle \mathbf{b}\mathbf{b}^{\mathrm{T}} \rangle$ is generally nonisotropic and geographically dependent we need to assume no correlation between elements, a priori. At 24° and 36°N, reference velocities are generally smaller than 0.2 cm s^{-1} in the oceanic interior while variability reaches approximately ± 0.5 cm s^{-1}

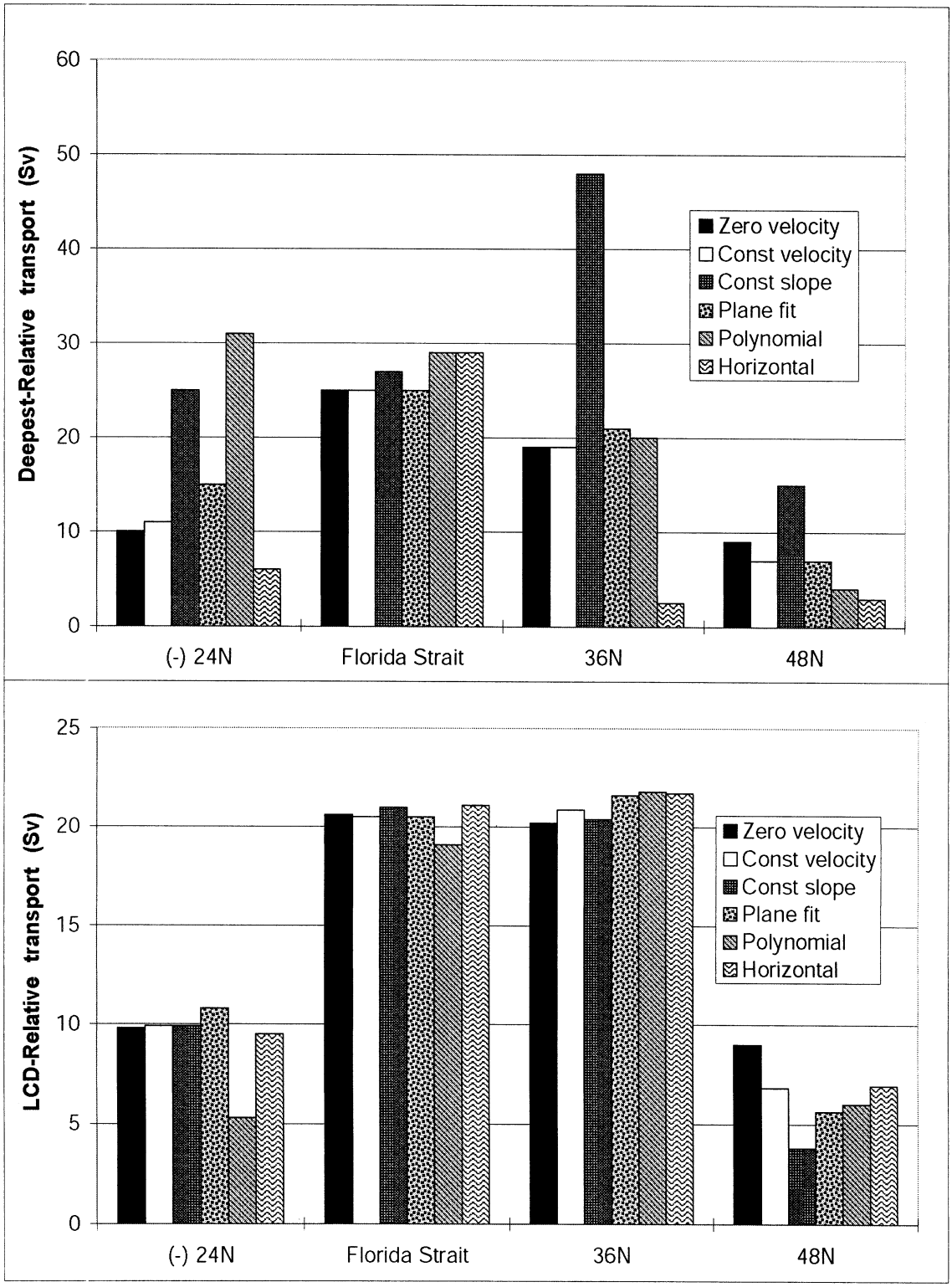

FIG. 6. Net relative transport across real hydrographic sections and for different bottom triangle extrapolations (the bars are in order as indicated by the legend). The calculation is much more sensitive to the method if the reference in shallow waters is taken at the (upper) deepest stations, than at the (lower) deepest common level. Note the different *y*-axis scales.

rms. The mean reference velocities increase to 20 cm s^{-1} near the western boundary and to 5 cm s^{-1} in shallow water farther east. At 48°N the amplitude of both mean and variability is twice as large in the oceanic interior, while mean velocities of up to only 6 cm s^{-1} are found in the deep western boundary current near the continental slope. This variability in the interior is insensitive to a deeper choice of reference isopycnal (3000–3600 versus 1200–2000 m).

It is not clear whether the correct prior variance for $\overline{b}$ should be the mean, the variability, or the rms. Variability is an overestimate, as it includes fast responses to Ekman transport fluctuations (section 3a). But it also includes baroclinic eddy contributions that could be necessary to $\overline{b}$ to produce a circulation that is consistent with the instantaneous realization $\upsilon_R(t)$. To first order, time mean and variability have similar magnitude, and because the GCM reproduces about half of the actual oceanic variability (section 3), an a priori value for the reference velocity variance in the interior of 1 $cm^2\ s^{-2}$ appears reasonable [Macdonald (1998) used such a value]. In shallow waters, near boundary currents, and in the vicinity of high shears, this value should be increased according, for instance, to current meter statistics where available. Because the initial circulation can be dramatically dependent upon the arbitrary choice of reference surface (e.g., Bryden and Beal 2001), the a priori size (or uncertainty) of the solution needs to be chosen accordingly so that the uncertainty of the circulation reflects this arbitrariness.

6. Silicate

Because, like most dissolved nutrients, silicate is depleted near the surface, its transports have a different spatial structure than that of mass transport. As a result, silicate conservation is a powerful constraint to increase the accuracy of ocean circulation determination. However, the weight attributed to silicate conservation remains approximate, with some authors requiring conservation at depths (Wunsch et al. 1983; Macdonald and Wunsch 1996) and others top to bottom (Robbins and Toole 1997; Ganachaud and Wunsch 2002). Based on published silicate measurements and our GCM, we review the rationale for silicate conservation.

In an attempt to quantify the global silica budget from the few existing measurements, Nelson et al. (1995) suggested that 50% of the global opal production is recycled in the euphotic zone, allowing a maximum global particle flux of 4500 kmol Si s^{-1} to enter the deep layers. Particles reaching the sea floor are partially buried, with an average global burial/production of 3%. The burial is believed to be almost negligible in the large oligotrophic regions (e.g., Tréguer et al. 1995) while it reaches a maximum of 5% in high-productivity regions such as the Southern Ocean [isotopic measurements from Joint Global Ocean Flux Study (JGOFS) Antarctic program; F. Sayles 2001, personal communication]. These estimates contradict previous beliefs that in the Southern Ocean up to 25% of the surface production was buried (DeMaster et al. 1991). Net sources and sinks of silicate appear to be much smaller than the biogenic fluxes. The global sink of silicate estimated from sediment data is about 220 kmol Si s^{-1} and close to the source from river runoff, at 160 kmol Si s^{-1} (Tréguer et al. 1995). Although little is known about them, hydrothermal activity, basaltic erosion, and eolian inputs are estimated at 40 kmol Si s^{-1} in total (Tréguer et al. 1995). Therefore, silica fluxes are to first order a vertical balance between surface particle export and deep or bottom remineralization in the water column. As a result, silicate is expected to be conservative when diagnosed within an oceanic area enclosed by hydrographic sections.

Three processes may limit the application to inverse models due to nonsteadiness or particle transports, namely, the erosion of the sea floor during a transient period, time changes in export production, and the horizontal advective transport of siliceous particles. To first order the transports do not appear to create large sources or sinks of dissolved silicate (appendix B). Within the limits of the present understanding of the silica cycle, dissolved silicate is expected to be top-to-bottom conservative within a few 10 kmol Si s^{-1}. We now examine the error due to baroclinic variability in silicate transport.

a. Variability in baroclinic silicate transports

As for mass, time variability in advective silicate transports introduces a noise $n^{\upsilon}_{\mathrm{Si}}$ in the time-mean silicate conservation equations. Variability in the meridional transport of silicate is not possible to estimate from existing observations, and our GCM does not contain any nutrient information. To proceed, an estimated silicate variable was created in the GCM by performing a regression of observed potential temperature and longitude with silicate. Figure 7 (left) shows the silicate concentration versus temperature in the Atlantic at 36°N. An analytical function was sought in the form of Chebyshev polynomials tapered with an exponential to remove the dominant vertical structure:

$$S_i(\theta, l) = \sum_{i=0}^{6} a_i T_i(\theta) e^{-10\times(\theta-1)} + a_7 \times l, \quad (16)$$

where S_i is the silicate concentration; l, θ are the longitude and the temperature scaled to the interval $[-1, 1]$; $T_i(t)$ is the ith Chebyshev polynomial (type 1); and the coefficients a_i are obtained by regression, independently on each side of the Mid-Atlantic Ridge. On the western side, the coefficients are $a_i = 10^{-3} \times$ [4.62 8.06 5.30 2.59 0.90 0.20 0.02 7.8]; while on the eastern side, $a_i = 10^{-3} \times$ [5.40 9.35 6.03 2.83 0.92 0.18 0.0175 1500]. Figure 7 (left) shows the corresponding curves and (right) the residuals. The residuals are small relative to mean con-

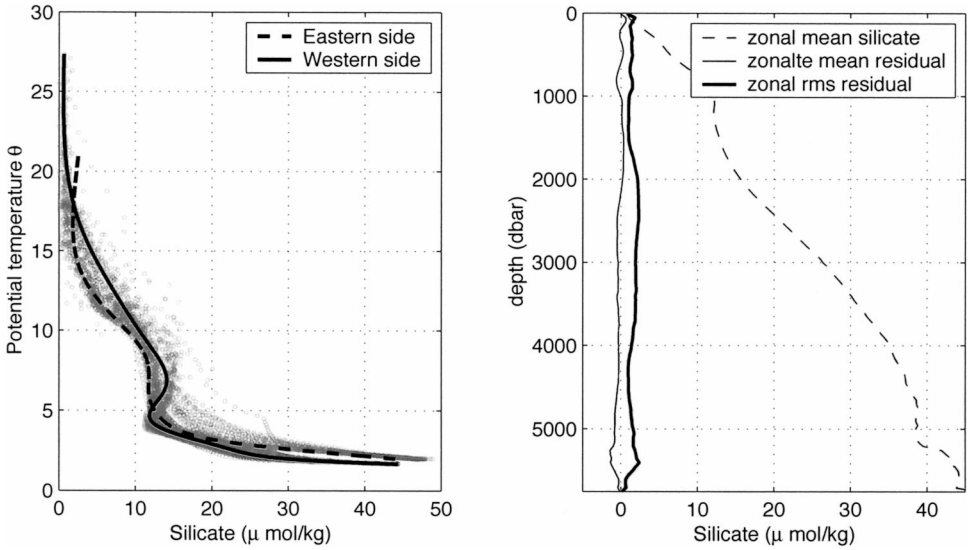

FIG. 7. (left) Silicate vs potential temperature at 36°N in the Atlantic. The solid line corresponds to the regressions obtained west of the Mid-Atlantic Ridge, while the dashed line corresponds to the data east of the ridge. The data points are given by the cloud of circles. (right) Silicate residual after regression at each depth. For comparison, the mean silicate concentration is overlaid. (The accuracy of very best routine measurements of silicate is 0.5–1.0 μmol kg^{-1}.)

centration, meaning that the function (16) adequately represents the field for polynomials of degree 6.

Using this analytical representation, the instantaneous silicate fields were computed from the GCM output temperature fields. A discontinuity arises above the mid-Atlantic ridge from the change in the regression function but does not introduce significant spurious variability. The geostrophic transport of silicate was obtained, as for the volume transport, every third day for 8 yr through our isopycnal layers (Table 1). Figure 8 shows the total thermal wind (T_R) transport and variability of silicate. In contrast with mass, the thermal wind variability of silicate $\langle (n_{\mathrm{Si}}^v)^2 \rangle$ does not vary substantially with depth, with about ± 10 kmol Si s^{-1} in each layer and ± 50 kmol Si s^{-1} top to bottom.

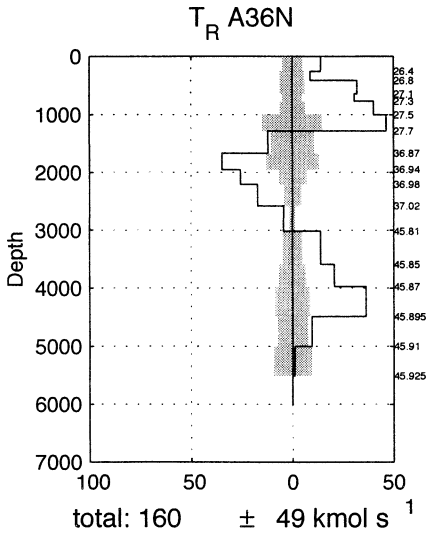

FIG. 8. Silicate variability at 36°N due to changes in the density field, T_R. The shaded area corresponds to the variability in each layer. The line gives the average relative transports through each layer in kmol Si s^{-1}.

Therefore, between two hydrographic sections in the North Atlantic, an a priori uncertainty of order 100 kmol Si s^{-1} appropriately accounts for aliasing and biogeochemical sources (river runoff, hydrothermal, dissolution) and sinks (burial) that are both much smaller than 100 kmol Si s^{-1}. Seasonal rectification effects were found important for nitrate by Williams and Follows (1998) at the edge of the subtropical gyre. For nitrate, this effect is weak in comparison with the magnitude of a posteriori uncertainties in inverse models (e.g., Ganachaud and Wunsch 2002), with about 4 kmol N s^{-1} (A. J. McLaren 1999, personal communication), and it is anticipated to be small for silicate too.

b. Silicate and anomaly equations

As described in Ganachaud et al. (2000) and other papers (e.g. Wijffels 1993; McIntosh and Rintoul 1997) there is an advantage to using anomaly equations for tracer conservation. Taking salt as an example, intuitively, mass and salt conservation equations are strongly correlated (the latter is about 35 times the former). For better conditioning of the system of equations, the mass conservation equation times an average salinity is subtracted from the salt conservation equation to form the so-called anomaly equation. The utility of this step is actually dependent not upon the relative magnitude of the equation coefficients (modern computer word

lengths have more than ample accuracy to accommodate observed mass and salinity distributions), but upon the assumption that the subtraction removes a strongly correlated noise term from the two original equations (Wunsch 1996, p. 273).

Anomaly equations turn out to be difficult to use for top-to-bottom silicate when spurious mass divergences occur in upper layers. The depth-average silicate concentration is higher than the upper-ocean concentration—where the top-to-bottom mass divergence actually occurs—so that subtracting the mass divergence times the depth-average silicate concentration may create an erroneous source or sink of silicate in the top-to-bottom anomaly equation. A solution to this problem is to use the sum of anomaly equations in individual layers for the top-to-bottom anomaly equations of silicate.

7. Summary and discussion

The different sources of noise in geostrophic linear inverse box models were examined in three midlatitude North Atlantic sections, and the following was found.

1) The high-frequency variability in transoceanic transports is dominated by fast, depth-independent responses to Ekman transport fluctuations. Consequently, linear inverse models can consistently combine different sections as long as the time-mean Ekman transport is used for all sections. The a priori uncertainty of mean Ekman transports probably lies in the range of 20%–50%.
2) The baroclinic shear relative to a deep reference surface is stable on large scales so that the relative transport measured at any one time is representative of the time mean. The residual error is not negligible, with a total of order ± 5 Sv at midlatitudes for the top-to-bottom transport and ± 0.1 to ± 2 Sv in the selected individual layers. The finite time required by a ship to cross the ocean does not significantly increase those values.
3) The measurement noise is dominated by internal wave vertical heave of isopycnals, implying a ± 3 Sv error in the transport estimates at midlatitudes. The geostrophic assumption and the bottom triangle issues induce smaller errors except in very specific situations such as a boundary current with large curvature or a deep boundary current against a slope.

Table 2 summarizes the a priori uncertainties on the top-to-bottom flow and on the flow in isopycnal layers above and below 2000 db. Assuming that the different kind of uncertainties are independent, the total rms in the top-to-bottom transport uncertainty is of ± 6 rms Sv. In a mass conservation equation involving two sections, the noise level, assuming uncorrelated errors between the sections (a coherence analysis showed no significant correlation at any time scale), would be of ± 8.5 Sv rms, suggesting a fourfold increase of the 2 Sv rms uncertainty adopted by previous authors (Rintoul and Wunsch 1991; Macdonald 1998). Using such an error for the net transport through a section is somewhat counterintuitive, as it is known, independently from inverse models and hydrographic data, that mass is conserved within the uncertainty of freshwater transport divergence, ± 1 Sv or less. But, for linear box inverse models with no adjustment to density, variability is aliased in one-time sections and produces spurious residuals in mass conservation. To account properly for those residuals in the error budget, it has been shown that one must accordingly enhance mass conservation at depth where the circulation is less variable, at the expense of the top-to-bottom conservation equation, as illustrated by Fig. 4. Failure to do so results in spurious inferred vertical transfers and underestimated uncertainties.

TABLE 2. Error budget at 36°N in the Atlantic (Sv rms).[a]

	Total[b]	Above 2000 m	Below 2000
Variability	5	1–2	0.5
Internal waves	3	—	0.2
Geostrophy[c]	2	—	—
Bottom wedge	1	—	—
Total error	6	1–2	0.5

[a] Those a priori uncertainties are provided for the total transport and in the layers of Table 1, above and below 2000 db.
[b] Uncertainty in the top-to-bottom transport.
[c] From the Gulf Stream curvature at 36°N.

Because silicate is a powerful tracer to constrain the circulation, the silicate transport errors were estimated along with mass. The aliasing of baroclinic variability from the GCM was estimated at ± 50 kmol Si s^{-1} rms top to bottom and at ± 10 kmol Si s^{-1} rms in individual layers. For two North Atlantic sections, a total uncertainty of ± 100 kmol Si s^{-1} appropriately accounts variability and biogeochemical sources and sinks.

The a priori reference velocity magnitude was evaluated from the GCM as lying between ± 0.5 and ± 1 cm s^{-1}. To represent the uncertainties due to the reference surfaces choice, the a priori values may be modified according to independent measurements and local shear. Shallow reference surfaces translate large eddy velocities in the upper ocean into large velocities at the bottom. The corresponding bottom transports are artificial and do not cancel unless the bottom is flat. Using a deep reference surface minimizes this error and is appropriate as long as an appropriate range of adjustment is allowed in the reference velocities.

The evaluation of the error from time variability is dependent upon the skill of the GCM. As was noted previously, the GCM underestimates observed variability by a factor of 2–4. However, we do not know the respective fractions of baroclinic and barotropic variability that are represented, nor could we evaluate the GCM skills at depth. Because the uncertainties that we derive are in agreement within a factor of 2 with an analysis from repeat hydrographic sections, it is be-

lieved that the estimates reported are sufficiently accurate for a priori uncertainties.

Uncertainties of vertical (diapycnal) transfers derive from the preceding error budget. Given their large spatial and temporal variability, and the nonexistence of large-scale measurements, a priori uncertainties on w^* and κ^* are large. The a priori size of w^* is determined by estimates of the horizontal circulation (e.g., 15-Sv upwelling in the Indian Ocean implies $w^* \simeq 0.5 \times 10^{-4}$ cm s^{-1}). For κ^*, microstructure measurement varies between 0.1 and 100 cm^2 s^{-1} (e.g., Polzin et al. 1997), with localized, high-mixing regions. Inverse models should allow large range over which to determine κ^* from the conservation equations.

A last component of the model error is the Eulerian nature of the transport calculation. Eulerian tracer motions are approximations of the true Lagrangian transports sought. The problem is too complex to be addressed in the present context and we are left with the assumption that the error implied does not greatly exceed the error from the variability.

One of the main objectives of hydrographic measurements is to estimate climate-related quantities such as the heat transport. If the circulation and uncertainties are calculated properly, any derived property transport and uncertainty will be correct. This, however, does not include processes such as seasonal rectification, which for heat transports was shown to be small north of 45°S and away from the equator (Jayne and Marotzke 2001).

What is the relevance of the preceding discussion to other oceanic regions? While measurement noise estimates are valid for any midlatitude regions, the present estimates for variability are specific to the North Atlantic Ocean. Ganachaud and Wunsch (2000) chose to extrapolate mass results to the global ocean, using a simple scaling by the Coriolis parameter (see Ganachaud 1999). The few existing observations suggest that variations in the measured geostrophic transports in other basins are similar to those of the Atlantic Ocean (e.g., Wijffels et al. 1996; Roemmich et al. 2001). In the Indian Ocean, model simulations give qualitatively similar results, with the variability being dominated by the barotropic response to Ekman transport changes (Lee and Marotzke 1998). Nevertheless, the logical extension of this work will be a generalization to all oceanic regions. Future work will also need to quantify uncertainties in anomaly equations and examine the case of sections crossing in midocean. Extrapolation of the silicate results to other oceans may be done, for instance, by scaling with the local Si concentration and local mass variability. This method assumes that larger Si concentrations are related to a larger vertical Si gradients and, therefore, to larger baroclinic variability in the Si transports (e.g., Ganachaud et al. 2000).

Acknowledgments. This work was completed as part of a Ph.D. thesis within the MIT–WHOI Joint Program in Physical Oceanography. Prof. Carl Wunsch provided valuable scientific advice and greatly helped improve the manuscript. Many conversations and comments from J. Toole, J. Marotzke, B. Warren were appreciated. B. King, an anonymous reviewer, A. Macdonald, P. Isachsen, H. Bryden, A. Hernandez, and P. Robbins provided valuable comments and suggestions. S. Jayne and R. Tokmakian made the GCM fields available. This work was supported in part at MIT by the Jet Propulsion Laboratory and the American Auto Manufacturers Association through the MIT Center for Global Change Sciences, and by the CNES.

APPENDIX A

Integrated Conservation Equation

One can integrate (3) over a layer bounded horizontally by two zonal hydrographic sections and land, and vertically between selected isopycnal surfaces, and rearrange the terms to obtain

$$\left[\int_{\text{West}}^{\text{East}} dx \int_{\text{Bot}(x)}^{\text{Top}(x)} dz\ \rho C v\right]_{\text{South}}^{\text{North}} = \left[\iint dx\ dy\left(\kappa\frac{\partial(\rho C)}{\partial z} - w\rho C\right)\right]_{\text{Bot}}^{\text{Top}} + Q, \quad \text{(A1)}$$

where $[X]_{\text{South}}^{\text{North}} \doteq X^{\text{North}} - X^{\text{South}}$, w is the velocity perpendicular to the top or bottom interface, κ is the dianeutral diffusivity, and the source Q is integrated over the layer. The left-hand side can be calculated from the velocities across the sections, but the right-hand side is not directly computable. The right-hand side is decomposed as follows, assuming that the second-order Reynolds terms are negligible:

$$\iint dx\ dy\left[\kappa\frac{\partial(\rho C)}{\partial z} - w\rho C\right] \simeq A\left[\kappa^*\frac{\overline{\partial(\rho C)}}{\partial z} - w^*\overline{\rho C}\right], \quad \text{(A2)}$$

where the horizontal overbar denotes a horizontal average; A is the horizontal area of a given neutral surface bounded by the sections; and w^*, κ^* represent the equivalent average dianeutral velocity and diffusivity across the interface. Such a formalism assumes for $\kappa^* > 0$ downgradient turbulent transports in the dianeutral direction. Both $\overline{\rho C}$ and $\overline{\partial(\rho C)}/\partial z$ are calculated from the section data, that is, at the boundaries of each ocean sector. Using (2) and (A2), (A1) may be written as

$$[T_b]_{\text{South}}^{\text{North}} + A\left[w^*\overline{\rho C} - \kappa^*\frac{\overline{\partial(\rho C)}}{\partial z}\right]_{\text{Bot}}^{\text{Top}} = [-T_R]_{\text{South}}^{\text{North}} + Q, \quad \text{(A3)}$$

where Q includes the freshwater transport in the mass budget and the Ekman transport divergence for all tracers including mass.

APPENDIX B

Nonconservative Silicate Processes

a. Time variability of opal rain

Deuser et al. (1995) observed a 50% decrease in opal rain over 20 yr in the Sargasso Sea. Because the residence time of opal is over 100 yr on the sea floor before dissolution (Sayles et al. 1996), such change can lead to an imbalance between yearly averaged opal rain and dissolution. The observed benthic dissolution is either similar to (Sayles et al. 1996) or lower than opal rain (Ragueneau et al. 2000), suggesting that such effect is not a primary issue.

b. Dissolution from a hypothetical seafloor erosion

In the steady state, it is believed that silica from opal rain is buried in the sediments; that is, there is a net opal flux to sediments. The burial can accumulate sediment at a rate of up to 17 cm $(\text{Kyr})^{-1}$ in the Southern Ocean (DeMaster 1981). A hypothetical net erosion would correspond to the reversal of accumulation during a (hypothetical) episodic event on climate timescales. For instance, a 100 kmol Si s^{-1} source over an area such as the North Atlantic between 24° and 36°N corresponds to an average erosion rate of 0.4 mol Si yr^{-1} m^{-2}. In this case, taking a sediment density of 0.4 g cm^{-3} (DeMaster 1981), with a 1.5% opal content (Sayles et al. 1996, p. 20), the seafloor erosion rate would be 4 m $(\text{Kyr})^{-1}$. Such an erosion, about 20 times the largest sedimentation rates, would be an alarming discontinuity in sediment records (T.-H. Peng 2001, personal communication), excluding the hypothesis of an erosion of such magnitude. Furthermore, direct measurements of the silicate flux from benthic chambers or pore water analysis are less than or equal to the measured rain rate, indicating a first-order steady-state balance between rain and benthic dissolution in most places, and a net accumulation (up to 2 mol Si yr^{-1} m^{-2}) in the Southern Ocean, unless particle transports in the nepheloid layer (layer of bottom particulate transports) dominate the budget (Ragueneau et al. 2000, Fig. 11).

c. Advection across sections

Horizontal advection of siliceous particles can potentially create an apparent net divergence of dissolved silicate. Few observations of particulate silica are available. The largest concentrations are observed in the Southern Ocean, with values for biogenic silica of up to 4 μmol L^{-1} at the surface, lower in the deep layers (0.2 μmol L^{-1}), and up to 2.6 μmol L^{-1} near the bottom (Tréguer et al. 1990). For a large surface current of 10 Sv, 1 μmol L^{-1} would correspond to a horizontal advective transport of 10 kmol Si s^{-1} of biogenic silica. Across a whole section, this transport should be the same order of magnitude as it is dominated by regions of simultaneous high productivity and strong currents. Although the effect cannot be totally ignored, particle advection is a priori smaller than the uncertainty of ± 100 kmol Si s^{-1} due to baroclinic variability [section 3b(1)]. (Within the steady-state assumption, strong particle advection would be associated with a large silicate depletion on one side of the section and an enrichment on the other side.)

REFERENCES

Arbic, B. K., and W. B. Owens, 2001: Climatic warming of Atlantic intermediate waters. *J. Climate,* **14,** 4091–4108.

Bryden, H., and L. Beal, 2001: Role of the Agulhas Current in Indian Ocean circulation and associated heat and freshwater fluxes. *Deep-Sea Res.,* **48A,** 1821–1845.

——, M. J. Griffiths, A. M. Lavin, R. C. Millard, G. Parrilla, and W. M. Smethie, 1996: Decadal changes in water mass characteristics at 24°N in the subtropical North Atlantic Ocean. *J. Climate,* **9,** 3162–3186.

Chereskin, T. K., and D. Roemmich, 1991: A comparison of measured and wind-driven Ekman transport at 11°N in the Atlantic Ocean. *J. Phys. Oceanogr.,* **21,** 869–878.

DeMaster, D. J., 1981: The supply and accumulation of silica in the marine environment. *Geochim. Cosmochim. Acta,* **45,** 1715–1732.

——, T. M. Nelson, S. L. Harden, and C. A. Nittrouer, 1991: The cycling and accumulation of biogenic silica and organic carbon in Antarctic deep-sea and continental margin environments. *Mar. Chem.,* **35,** 489–502.

Deuser, W. G., T. D. Jickells, P. King, and J. A. Commeau, 1995: Decadal and annual changes in biogenic opal and carbonate fluxes in the deep Sargasso Sea. *Deep-Sea Res.,* **42,** 1923–1932.

Fieux, M., R. Molcard, and A. G. Ilahude, 1996: Geostrophic transport of the Pacific–Indian Oceans throughflow. *J. Geophys. Res.,* **101,** 12 421–12 432.

Ganachaud, A., 1999: Large scale oceanic circulation and fluxes of freshwater, heat, nutrients and oxygen. Ph.D. thesis, Massachusetts Institute of Technology/Woods Hole Oceanographic Institute Joint Program, 267 pp.

——, and C. Wunsch, 2000: The oceanic meridional overturning circulation, mixing, bottom water formation and heat transport. *Nature,* **408,** 453–457.

——, and H. Mercier, 2002: Ocean response to meridional Ekman transport in the Atlantic and implication for gravity missions. *Geophys. Res. Lett.,* **29,** 2145, doi:10.1029/2002GL015291.

——, and C. Wunsch, 2002: Oceanic nutrient and oxygen transports and bounds on export production during the World Ocean Circulation Experiment. *Global Biogeochem. Cycles,* **16,** 1057, doi: 10.1029/2000GB001333.

——, ——, J. Marotzke, and J. Toole, 2000: The meridional overturning and large-scale circulation of the Indian Ocean. *J. Geophys. Res.,* **105,** 26 117–26 134.

Garrett, C., and W. Munk, 1972: Space–time scales of internal waves. *Geophys. Fluid Dyn.,* **3,** 225–264.

Gill, A. E., 1982: *Atmospheric–Ocean Dynamics.* Academic Press 662 pp.

——, and P. P. Niller, 1973: The theory of seasonal variability in the ocean. *Deep-Sea Res.,* **20,** 141–178.

Jayne, S. R., and R. Tokmakian, 1997: Forcing and sampling of ocean general circulation models: Impact of high-frequency motions. *J. Phys. Oceanogr.,* **27,** 1173–1179.

——, and J. Marotzke, 2001: The dynamics of ocean heat transport variability. *Rev. Geophys.,* **39,** 385–411.

Johns, E., D. R. Watts, and H. T. Rossby, 1989: A test of geostrophy in the Gulf Stream. *J. Geophys. Res.,* **94,** 3211–3222.

Joyce, T., and C. Corry, 1994: WOCE operations manual. Woods

Hole Oceanographic Institiution, Tech. Rep. WOCE report No. 67/91/WHPO publication 90–1, Revision 2, 144 pp.
Koltermann, K. P., A. Sokov, V. Terechtchencov, S. Dobroliubov, K. Lorbacher, and A. Sy, 1999: Decadal changes in the thermohaline circulation of the North Atlantic. *Deep-Sea Res.*, **46B,** 109–138.
Lavin, A., 1993: Climatic changes in temperature and salinity in the subtropical North Atlantic. M. S. thesis, Dept. of Earth, Atmospheric and Planetary Sciences, Massachusetts Institute of Technology, 126 pp.
Lee, T., and J. Marotzke, 1998: Seasonal cycles of meridional overturning and heat transport of the Indian Ocean. *J. Phys. Oceanogr.,* **28,** 923–943.
Levitus, S., and T. P. Boyer, 1994: *Temperature.* Vol. 4, *World Ocean Atlas 1994,* NOAA Atlas NESDIS 4, 117 pp.
——, R. Burgett, and T. Boyer, 1994. *Salinity.* Vol. 3, *World Ocean Atlas 1994,* NOAA Atlas NESDIS 3, 99 pp.
Levy, M., P. Klein, and A.-M. Tréguier, 2001: Impacts of sub-mesoscale physics on phytoplancton production and subduction. *J. Mar. Res.,* **59,** 535–565.
Luyten, J., H. Stommel, and C. Wunsch, 1985: A diagnostic study of the northern Atlantic subpolar gyre. *J. Phys. Oceanogr.,* **15,** 1344–1348.
Macdonald, A., 1998: The global ocean circulation: A hydrographic estimate and regional analysis. Progress in Oceanography, Vol. 41, Pergamon, 281–382.
——, and C. Wunsch, 1996: An estimate of global ocean circulation and heat fluxes. *Nature,* **382,** 436–439.
Marotzke, J., and J. Willebrand, 1996: The North Atlantic mean circulation: Combining data and dynamics. *The Warmwatersphere of the North Atlantic Ocean,* W. Krauss, Ed., 55–90.
McDougall, T., 1987: Neutral surfaces. *J. Phys. Oceanogr.,* **17,** 1950–1964.
McIntosh, P. C., and S. R. Rintoul, 1997: Do inverse box models work? *J. Phys. Oceanogr.,* **27,** 291–308.
Mercier, H., 1986: Determining the general circulation of the ocean: A nonlinear inverse problem. *J. Geophys. Res.,* **91,** 5103–5109.
Mestas-Nuñez, A. M., D. B. Chelton, M. H. Freilich, and J. G. Richman, 1994: An evaluation of ECMWF-based climatological wind-stress fields. *J. Phys. Oceanogr.,* **24,** 1532–1549.
Munk, W., 1981: Internal waves. *Evolution of Physical Oceanography, Scientific Surveys in Honor of Henry Stommel,* B. A. Warren and C. Wunsch, Eds., The MIT Press, 264–291.
Nelson, D. M., P. Tréguer, M. A. Brezezinski, A. Leynaert, and B. Queguiner, 1995: Production and dissolution of biogenic silica in the ocean: Revised global estimates, comparison with regional data and relationship to biogenic sedimentation. *Global Biogeochem. Cycles,* **9,** 359–372.
Pedlosky, J., 1987: *Geophysical Fluid Dynamics.* 2d ed. Springer-Verlag, 710 pp.
Polzin, K. L., J. M. Toole, G. R. Ledwell, and R. W. Schmitt, 1997: Spatial variability of turbulent mixing in the abyssal ocean. *Science,* **276,** 93–96.
Ragueneau, O., and Coauthors, 2000: A review of the Si cycle in the modern ocean: Recent progress and missing gaps in the application of biogenic opal as a paleoproductivity proxy. *Global Planet. Change,* **26,** 317–365.
Rintoul, S. R., and C. Wunsch, 1991: Mass, heat, oxygen and nutrient fluxes and budget in the North Atlantic Ocean. *Deep-Sea Res.,* **38,** Suppl., 355–377.
Ripa, P., 1997: ''Inertial'' oscillations and the β-plane approximation(s). *J. Phys. Oceanogr.,* **27,** 633–647.
Robbins, P. E., and J. M. Toole, 1997: The dissolved silica budget as a constraint on the meridional overturning circulation in the Indian Ocean. *Deep-Sea Res.* **44A,** 879–906.
Roemmich, D., 1980: The application of inverse methods to problems in ocean circulation. Ph.D. thesis, Massachusetts Institute of Technology/Woods Hole Oceanographic Institution, 193 pp.
——, and C. Wunsch, 1985: Two transatlantic sections: Meridional circulation and heat flux in the subtropical North Atlantic Ocean. *Deep-Sea Res.,* **32,** 119–664.
——, J. Gilson, B. Cornuelle, and R. Weller, 2001: The mean and time-varying meridional transport of heat at the tropical/subtropical boundary of the North Pacific Ocean. *J. Geophys. Res.,* **106,** 8957–8970.
Saunders, P. M., 1986: Accuracy of measurement of salinity, oxygen, and temperature in the deep ocean. *J. Phys. Oceanogr.,* **16,** 189–195.
Sayles, F. L., W. G. Deuser, J. E. Goudreau, W. H. Dickinson, T. D. Jickells, and P. King, 1996: The benthic cycle of biogenic opal at the Bermuda Atlantic Time Series site. *Deep-Sea Res.,* **43,** 383–409.
Schludlich, R. R., and J. F. Price, 1998: Observations of seasonal variation in the Ekman layer. *J. Phys. Oceanogr.,* **28,** 1187–1204.
Semtner, A. J., and R. M. Chervin, 1992: Ocean general circulation from a global eddy-resolving model. *J. Geophys. Res.,* **97,** 5493–5550.
Stammer, D., R. Tokmakian, A. Semtner, and C. Wunsch, 1996: How well does a 1/4° global circulation model simulate large scale oceanic observations? *J. Geophys. Res.,* **101,** 25 779–25 811.
Tréguer, P., D. Nelson, S. Gueneley, C. Zeyons, J. Morvan, and A. Buma, 1990: The distribution of biogenic and lithogenic silica and the compostion of particulate organic matter in the Scotia Sea and the Drake Passage during autumn 1987. *Deep-Sea Res.,* **37,** 833–852.
——, D. M. Nelson, A. J. van Bennekom, D. J. DeMaster, A. Leynaert, and B. Quéguiner, 1995: The silica balance in the World Ocean: A re-estimate. *Science,* **268,** 375–379.
Tsimplis, M. N., S. Bacon, and H. L. Bryden, 1998: The circulation of the sub-tropical South Pacific derived from hydrographic data. *J. Geophys. Res.,* **103,** 21 443–21 468.
Wijffels, S. E., 1993: Exchanges between hemispheres and gyres: A direct approach to the mean circulation of the equatorial Pacific. Ph.D. thesis, Massachusetts Institute of Technology/Woods Hole Oceanographic Institute Joint Program, 297 pp.
——, J. M. Toole, H. L. Bryden, R. A. Fine, W. J. Jenkins, and J. L. Bullister, 1996: The water masses and circulation at 10°N in the Pacific. *Deep-Sea Res.,* **43,** 501–544.
Willebrand, J., S. G. H. Philander, and R. C. Pacanowski, 1980: The oceanic response to large-scale atmospheric disturbances. *J. Phys. Oceanogr.,* **10,** 411–429.
Williams, R. G., and M. J. Follows, 1998: The Ekman transfer of nutrients and maintenamce of new production over the North Atlantic. *Deep-Sea Res.,* **45,** 461–489.
Wunsch, C., 1978: The North Atlantic general circulation west of 50°W determined by inverse methods. *Rev. Geophys. Space Phys.,* **16,** 583–620.
——, 1994: Dynamically consistent hydrography and absolute velocity in the eastern North Atlantic Ocean. *J. Geophys. Res.,* **99,** 14 071–14 090.
——, 1996: *The Ocean Circulation Inverse Problem.* Cambridge University Press, 437 pp.
——, D. Hu, and B. Grant, 1983: Mass, heat, salt and nutrient fluxes in the South Pacific Ocean. *J. Phys. Oceanogr.,* **13,** 725–753.
Zhang, H.-M., and N. Hogg, 1996: Deducing dynamic properties from simulated hydrographic data. Part I: Results from a non-eddy-resolving model. *J. Mar. Res.,* **54,** 679–703.